

Pixel-wise Distance Regression for Glacier Calving Front Detection and Segmentation

Amirabbas Davari*, Christoph Baller*, Thorsten Seehaus, Matthias Braun, Andreas Maier, Vincent Christlein

Abstract—Glacier calving front position (CFP) is an important glaciological variable. Traditionally, delineating the CFPs has been carried out manually, which was subjective, tedious and expensive. Automating this process is crucial for continuously monitoring the evolution and status of glaciers. Recently, deep learning approaches have been investigated for this application. However, the current methods get challenged by a severe class-imbalance problem. In this work, we propose to mitigate the class-imbalance between the calving front class and the non-calving front class by reformulating the segmentation problem into a pixel-wise regression task. A Convolutional Neural Network gets optimized to predict the distance values to the glacier front for each pixel in the image. The resulting distance map localizes the CFP and is further post-processed to extract the calving front line. We propose three post-processing methods, one method based on statistical thresholding, a second method based on conditional random fields (CRF), and finally the use of a second U-Net. The experimental results confirm that our approach significantly outperforms the state-of-the-art methods and produces accurate delineation. The Second U-Net obtains the best performance results, resulting in an average improvement of about 21 % dice coefficient enhancement.

Index Terms—distance map regression, glacier calving front segmentation, SAR imagery, U-Net, class-imbalance

I. INTRODUCTION

Many glaciers are draining directly into the ocean or lakes (calving glaciers). In particular along the Antarctic Peninsula, in Patagonia or along Greenlands margins, the ice bodies are discharging ice via outlet glaciers, which are typically located in narrow fjords. The ice front position of calving glaciers can vary significantly and impact the ice dynamics. The retreat of the ice front can reduce the lateral buttressing forces or detach the ice from pinning points (bedrock) and thus destabilize the ice flow and cause further ice front recession [1]. For example, the retreat and disintegration of ice shelves along the Antarctic Peninsula has led to a sharp increase in ice discharge from tributary glaciers, causing an acceleration of glacier thinning, further retreat, and consequently high ice mass losses [2], [3].

Changes in the ice front position can also be linked to variations in the grounding zone (transition zone where a calving glacier starts to float) [4]. Deeper bedrock elevations

inland from the grounding zone (retrograde bedrock) will lead to a feedback mechanism called marine ice-sheet instability as the grounding zone retreats, resulting in further grounding zone retreat and increasing ice loss [5]. Therefore, monitoring of glacier front positions can serve as an indicator for changes in ice dynamics and provides crucial information for analyzing the ongoing processes, e. g., for model initialization or calibration.

Optical and SAR remote sensing imagery are typically used to map the position of the glacier front [6]. However, cloud cover and polar night limit the coverage by optical imagery, which is not the case for SAR data. Up to now, visual inspection and manual mapping of the glacier front is commonly used. In polar regions, the water in front of the glacier front is frequently covered by the so-called ice-mélange, consisting of sea ice and icebergs, which can look quite similar to a glacier surface on remote sensing imagery. Thus, the analyst needs to carefully separate between the ice-mélange and the actual glacier, making the analysis difficult and laborious. Moreover, such human analyses are always subjective and can vary from analyst to analyst [7]. Several semi-automatic and automatic ice front mapping techniques were developed, which typically rely on edge enhancement, image classification or edge detection. Baumhoer *et al.* [6] provide a detailed review of the various methods on this topic.

Recently, the first studies on using Convolutional Neural Networks (CNN) for glacier front mapping appeared. Mohajerani *et al.* [8] trained and tested a U-Net architecture on multi-spectral Landsat 5, 7, and 8 acquisitions at four outlet glaciers of the Greenland ice sheet. In a similar way, Baumhoer *et al.* [9] and Zhang *et al.* [10] mapped the ice fronts on SAR imagery from Sentinel-1 and TerraSAR-X. Both studies classify the surface region pixel-wise into the two types, i. e., ice mélange and non-ice mélange, and extract the final calving front position (CFP) in a post-processing step using edge detection algorithms.

A direct prediction of the glacier CFP is very challenging as the actual front line that the model should learn to predict contributes a very small portion to the number of image pixels. This leads to a severe class-imbalance, which is known to be an Achilles heel for supervised learning algorithms. While predicting the calving front lines directly, Mohajerani *et al.* [8] tackled the class-imbalance problem using a custom sample weight that penalizes miss-classified pixels of the calving front higher. In the medical image processing domain, applications like segmenting the optic disc (OD) and fovea in retinal images struggle with the class-imbalance problem, too. Meyer *et al.* [11] proposed to tackle this problem by reformulating the segmentation task to a pixel-wise regression that jointly detects OD and fovea location in a retinal image. The method

A. Davari, C. Baller, A. Maier and V. Christlein are with the Computer Science Department at Friedrich-Alexander University Erlangen-Nürnberg, 91058 Erlangen, Germany (email: amir.davari@fau.de).

T. Seehaus and M. Braun are with the Geography and Geosciences Department at Friedrich-Alexander University Erlangen-Nürnberg, 91058 Erlangen, Germany.

* Amirabbas Davari and Christoph Baller contributed equally to this work.

Grateful acknowledgment is made to the German Aerospace Center (DLR), the European Space Agency (ESA), and the Alaska Satellite Facility (ASF) for providing the SAR data for our analysis.

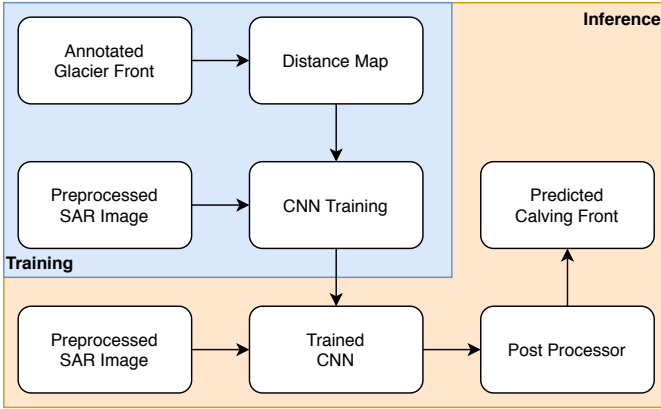


Fig. 1: Outline of our proposed workflow for automated calving front position segmentation.

achieved high detection results close to the human observer performance.

In this paper, we propose a strategy for glacier front segmentation using a modified U-Net with a similar architecture used by Zhang *et al.* [10], which is adjusted for semantic segmentation of SAR imagery. Getting inspired by Meyer *et al.* [11], we first reformulate the segmentation problem into a pixel-wise regression task and train the U-Net to predict the distance map transform of the glacier fronts in the SAR images. The output of this step is not only accurate and robust against the class-imbalance, but also emphasizes the region of interest, i. e., the glacier front line and can serve for detection purposes and human annotation. In the next step, in an attempt to automatically extract the actual glacier front locations from the predicted distance maps, we propose the use of three distinct approaches, namely statistical threshold, a conditional random field, and a second U-Net. The rest of the presentation in this paper is organized as follows: Section II reviews the tools used in this work and explains the proposed algorithms. Section III is dedicated to demonstrating the dataset, explaining the evaluation setup, and presenting and discussing the quantitative and qualitative results. Finally, Section IV concludes the paper and discusses the outlook.

II. METHODOLOGY

Figure 1 depicts the overview of our proposed workflow. It consists of three key processing blocks: the distance map transform, CNN training, and post-processing. This section is dedicated to explaining these blocks in detail.

A. Distance Map Transform

Glacier front detection can be described as a semantic image segmentation problem that is usually resolved by a binary classification, where the classes are determined pixel-wise by their affiliation to the glacier front. The problem is the high imbalance between the frequencies of the glacier front class and non-glacier front class samples, which significantly challenges the optimization of the model. To mitigate this issue, we propose to follow Meyer *et al.* [11] and reformulate the semantic segmentation problem at hand into a regression task,

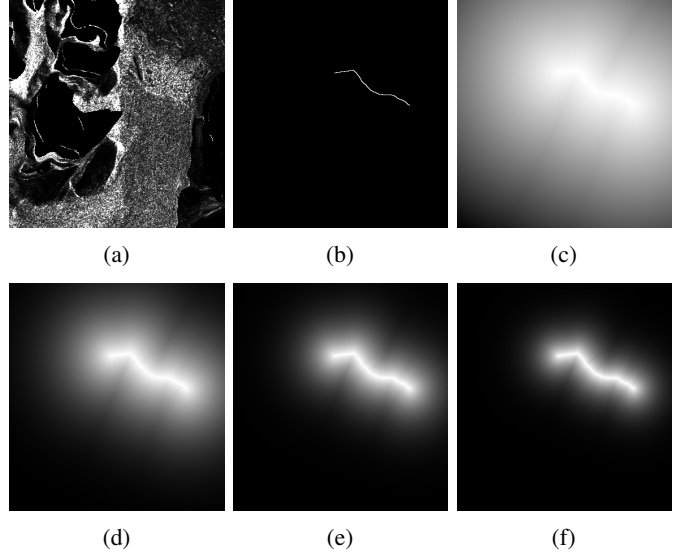


Fig. 2: (a) Sample SAR image from the Mapple glacier (ENVISAT 2010-07-03), (b) glacier calving front position ground truth, (c)–(f) corresponding ground truth distance map with $\gamma \in \{1, 4, 7, 10\}$.

where the model approximates the closeness of each pixel in the image to the glacier front line.

The distance map for each pixel $p(x, y) \in \Omega$ represents the distance to the glacier front, where $\Omega \subset \mathbb{R}^2$ denotes the image domain. For each image in the dataset, we first binarize the ground truth calving front line, invert it so that the glacier front forms the background, and then apply the Euclidean distance transform (EDT).

$$D(x, y) = \text{EDT}(\text{invert}(p(x, y))) \quad (1)$$

Afterwards, we normalize the distance map D , where the pixel intensities decrease relative to their distance from the glacier front location;

$$D_{\text{norm}}(x, y) = \left(1 - \frac{D(x, y)}{\max D(x, y)}\right)^\gamma, \quad (2)$$

where γ is a decay parameter determining the spread of D_{norm} . The influence of the decay parameter is visualized in Fig. 2.

B. Deep Convolutional Neural Network

In order to transform the initial pixel-wise binary classification problem into a regression task, we need to train a model capable of accurately approximating $D_{\text{norm}}(x, y)$ given a Glacier SAR image. Convolutional Neural Networks (CNN) have revolutionized image analysis and computer vision domains. This work uses a CNN with a U-Net architecture [12], which has successfully been used for biomedical image segmentation. The U-Net consists of a contraction path followed by an expansion path that is connected via skip-connections. Our model is inspired by Zhang *et al.* [10], who adjusted the U-Net architecture for semantic segmentation of SAR imagery. The SAR images are the input for the model. The optimization process tries to minimize the mean squared error (MSE) loss

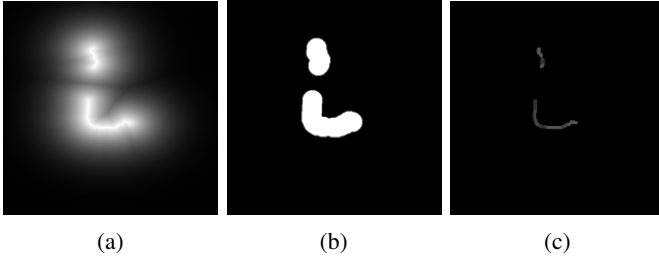


Fig. 3: Statistical Thresholding post processing steps: (a) predicted distance map, (b) binarized distance map, and (c) calving front line.

between the output of the neural network and the distance map transform of the corresponding glacier front mask of the input.

C. Post processing

The model predicts a smooth distance map, where the pixel intensities increase the closer they are to the glacier front. This map helps to localize the calving front line and narrows down the searching area for the region of interest. In the next step, the actual glacier calving front line should be extracted from the estimated distance map. Computing the maximum pixel intensity results in some sparse and noisy points that do not represent the CFP at all. In this work, we propose three different approaches to approximate the location of the glacier front, namely statistical thresholding, conditional random fields using guided filters, and a second U-Net as a learning-based approach.

1) *Statistical Thresholding (Threshold)*: Probably, the most intuitive solution to this problem is to threshold the distance map on a specific value. The prediction gets divided into two classes, one of which includes the glacier front line. Very small threshold values result in many false alarms while too large threshold values result in the exclusion of the correct CFP pixel and hence a severely discrete line. Furthermore, the pixel intensity value range in the predicted distance maps marking the CFPs vary for different SAR images. Therefore, the threshold needs to be adaptive and be selected for each image individually. To achieve this, we create a histogram of the distance map, which contains the quantity of all pixel intensities. We chose the threshold such that 95% of the intensity bins are belonging to the background. This ensures the extraction of a narrow region in the image containing the glacier front and not being polluted by too many false alarms. To further prune this area, we apply morphological thinning operation producing a skeleton that defines the final calving front line. Figure 3 illustrates these steps for a sample test data.

2) *Conditional Random Field*: Deep Convolutional Neural Networks tend to yield smooth responses. They can predict the presence and rough position of objects during the image segmentation but have difficulties to outline their borders and specifically sharp edges. To mitigate this problem, the location accuracy of a fully connected Conditional Random Field (CRF) in combination with the Neural Network was purposed in the DeepLab system [13]. With this approach, we use the same

strategy on our predicted distance maps. The CRF model employs the energy function

$$E(x) = \sum_i \theta_i(x_i) + \sum_{ij} \theta_{ij}(x_i, x_j) \quad (3)$$

with the unary potential $\theta_i(x_i) = -\log P(x_i)$, where $P(x_i)$ is the individual label assignment probability of the distance map model, $\theta_{ij}(x_i, x_j)$ is the pairwise potential, and x is the final label assignment for the pixel. We build the foreground and background classes of $P(x_i)$ by setting the background class probabilities as the inverse of the individual foreground class probability. The pairwise potential consists of a bilateral and a Gaussian kernel

$$\theta_{ij}(x_i, x_j) = \mu(x_i, x_j) \left[\omega_1 \exp\left(-\frac{\|p_i - p_j\|^2}{2\sigma_\alpha^2} - \frac{\|I_i - I_j\|^2}{2\sigma_\beta^2}\right) + \omega_2 \exp\left(-\frac{\|p_i - p_j\|^2}{2\sigma_\gamma^2}\right) \right], \quad (4)$$

where θ denotes the simple label compatibility function that is given by Potts model $\theta_{ij}(x_i, x_j) = [x_i \neq x_j]$, which only penalize nodes with distinct labels. The kernel potentials depend on pixel positions p and grayscale intensities I . The parameters σ_α , σ_β , and σ_γ control the scale of the Gaussian kernels and the linear combination weights ω_1 , ω_2 manage the individual influence of the kernel potentials. Thus, the CRF model efficiently approximates the probabilistic inference using Gaussian filtering in feature space [14]. This results in a specific class assignment of the calving front given the probabilities from the predicted distance map and its associated SAR image.

3) *Second U-Net*: Convolutional Neural Networks are successful and widely used to tackle today's computer vision problems. As described before, extracting the calving front line from the estimated distance map is challenging for various reasons, which can be tackled within a semantic segmentation regime using a U-Net. The output of the pixel-wise regression model in the first step of the workflow has the same dimension and shape as the original input and can be utilized as the input for a new segmentation model in the post-processing step.

In this approach, we use a second U-Net that takes the previously estimated distance maps and predicts the final glacier front. The neural network shares the same U-Net architecture we introduced in Section II-B. In order to train the model, we first reduce the still existing class-imbalance by thickening the glacier front lines using morphological dilation, which would otherwise substantially degrade the model optimization capabilities. We use the binary cross-entropy (BCE) loss function to calculate the difference between the predicted line and the ground truth glacier front mask.

III. EVALUATION

A. Dataset

1) *Study Sites*: We selected outlet glaciers at the Antarctic Peninsula (AP) to train and evaluate the glacier front mapping on SAR intensity imagery using CNN. The AP is a hot spot of global climate change. A significant temperature increase was reported for the 20th century [15], [16] strongly affecting

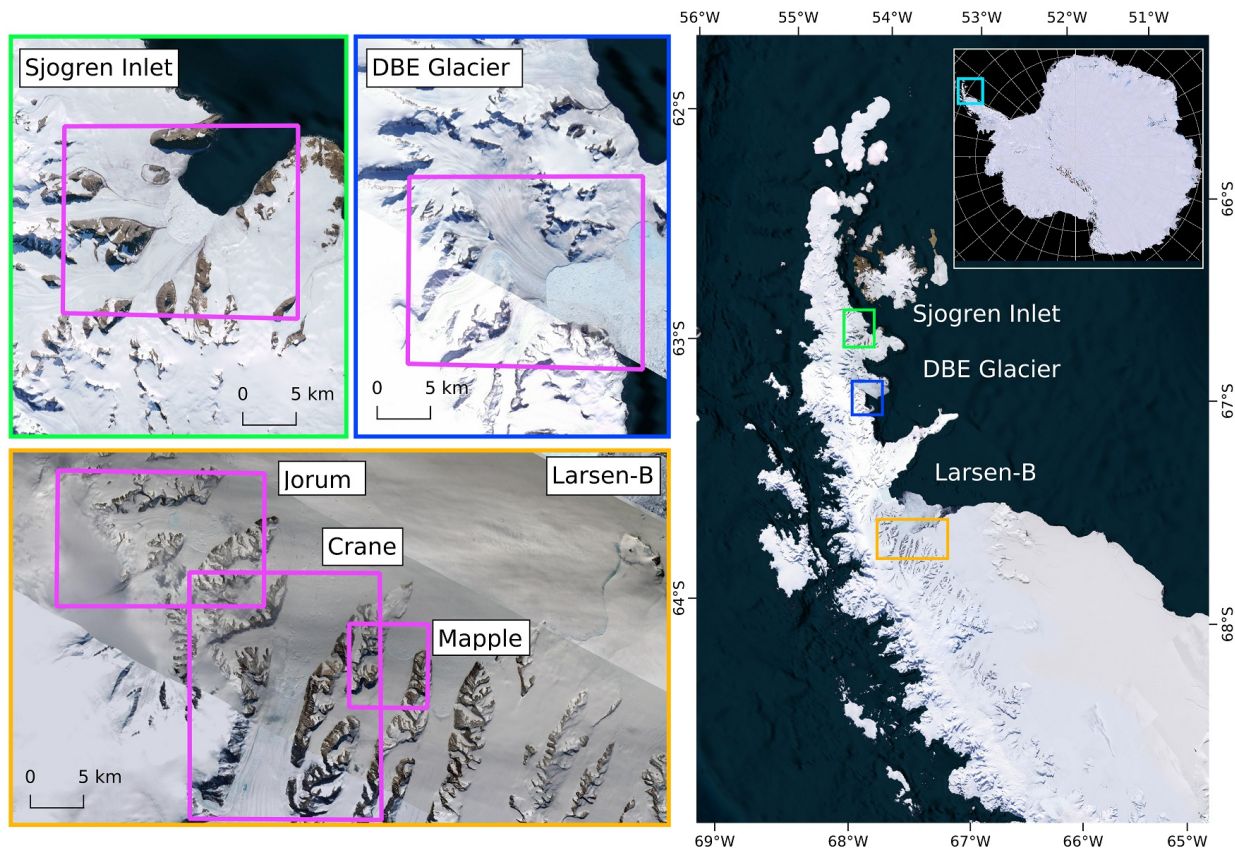


Fig. 4: Overview of studied glaciers on the northern Antarctic Peninsula. Pink polygons indicate the subsets used in the analysis. Background: Bing Aerial Maps © Microsoft and Google Maps © Google; Map of Antarctica: Landsat LIMA Mosaic © USGS, NASA, BAS, NFS.

its ice masses. Pronounced retreat and even disintegration of some ice shelves along the AP was observed [17]. Most of the northern ice shelves at the Prince-Gustav-Channel (PGC) and Larsen-A embayment disintegrated in 1995, and at the Larsen-B embayment in 2002 [3], [18], [19]. The reduction of the buttressing forces led to a strong increase in ice discharge and further frontal retreat of the former ice shelf tributary glaciers [20], [21]. Due to its relevance and the data availability, we selected several of these former ice shelf tributaries for our analysis (see Fig. 4).

The glacier system of the Sjøgren-Inlet (SI) and Dinsmoore-Bombardier-Edgworth (DBE) glacier systems were major tributaries to the PGC and Larsen-A ice shelves, respectively. Seehaus *et al.* [21], [22] carried out a detailed analysis of the glacier evolution after the disintegration of the ice shelves. Simultaneously, the glacier fronts strongly retreated after the ice shelf disintegration and stabilized at SI glacier system after about 15 years, whereas at DBE, the glacier re-advance and short-term recession was observed. Crane, Mapple and Jorum glaciers are former tributaries of the Larsen-B ice shelf. Rott *et al.* reported a similar reaction to the ice shelf break-up as DBE and SI glacier systems [20], [23].

We used imagery from the satellite missions ERS-1/2, Envisat, RadarSAT-1, ALOS, TerraSAR-X (TSX) and TanDEM-X (TDX), covering the period 1995–2014. The German Aerospace Center (DLR), the European Space Agency (ESA)

and the Alaska Satellite Facility (ASF) provided the SAR data for our analysis, via granted data proposals. The SAR acquisitions were multilooked to reduce speckle noise and calibrated. The ASTER digital elevation model of the AP [24] was used for the geocoding and the orthorectification of the images. The specifications and parameters of the SAR sensors and imagery are provided in Table I. The GAMMA RS Software was used for processing the imagery.

2) *Data Generation:* The manually annotated calving front positions for the DBE and SI glacier systems have been generated and used by Seehaus *et al.* [21], [22]. Additionally, we manually annotated the glacier front positions of the Larsen-B embayment. Figure 5 depicts the ice mélange and glaciers at the non-ice mélange regions (referred to as *zone* in this work), and the glacier calving front (referred to as *line* in this work) ground truth images for a sample SAR image in our dataset.

A quality factor, ranging from 1 to 6, was assigned to each SAR image. The quality factors are a subjective measure of the reliability of the picked front position depending on the similarity of the ice mélange and the glacier, with 1 being the most reliable and 6 the most unreliable. Table II shows the quality factors and the respective uncertainty values, perpendicular to the glacier front. In this study, we discarded the glacier fronts with a quality factor of 6.

Subsets of the preprocessed SAR intensity imagery were generated covering the areas of interest (see Fig. 4) and

TABLE I: Overview of the SAR sensors and specifications used to acquire the SAR images of the Antarctic Peninsula dataset.

Platform	Sensor	Mode	SAR band	Repetition cycle [d]	Time interval	Multi looking factor	Ground range resolution [m]
ERS-1/2	SAR	IM	C band	35/1	13. November 1995 - 26. February 2010	1x5	20
RADARSAT 1 (SLC & PRI format)	SAR	ST	C band	24	10. September 2000 - 20. January 2008	1x4	20 (SLC) 12.5 (PRI)
Envisat	ASAR	IM	C band	35	05. December 2003 - 03. July 2010	1x5	20
ALOS	PALSAR	FBS	L band	46	18. May 2006 - 03. March 2011	2x5	16,7
TerraSAR-X TanDEM-X (SLC format)	SAR	SM	X band	11	13. October 2008 - 22. December 2014	3x3	6.7

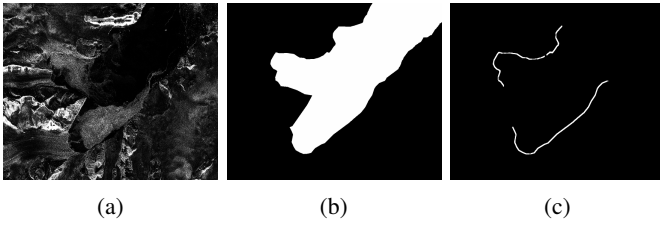


Fig. 5: Statistical Thresholding post-processing steps: (a) predicted distance map, (b) binarized distance map, and (c) calving front line.

Quality factor	1	2	3	4	5	6
$\sigma_f(m)$	70	130	200	230	450	-

TABLE II: Quality factors of manual glacier front detection and the assigned horizontal accuracies σ_f (perpendicular to estimated glacier front line).

converted to 16-bit single-channel images. Each manually picked glacier front position (spatial line) was combined with the coastline and rock-outcrop polygons (based on the Antarctic Digital Database at the AP) to generate a categorized 8bit single-channel image. The ground truth images have the same size and resolution as the respective SAR image subsets and are used for training the models.

B. Experiments

First, we compute the distance maps from the glacier front lines (ground truth). We set the decay parameter $\gamma = 7$, which produced the best result within the set $\gamma \in \{1 \dots 10\}$. The same decay value is also used by Meyer *et al.* [11]. The SAR images and the distance maps are then resized to 512×512 using linear interpolation and used as input for the first U-Net. The contraction path consists of five down-sampling steps with two 5×5 convolutional layer, each followed by a batch normalization layer and leaky rectified linear unit (Leaky ReLU) activation function, as well as a 2×2 max pooling operation. Each block of the expansion path uses a 4×4 transposed convolution layer with a stride of 2×2 that gets concatenated with the corresponding feature map

of the contracting path. Then the concatenation result goes through the same combination of two 5×5 convolutional layers, batch normalization layers, and Leaky ReLUs analogous to the contraction path. The number of the convolutional filters gets doubled with each down-sampling step from 32 to 1024, and correspondingly halved in each up-sampling step from 1024 to 32. The final layer is a 3×3 convolution layer with a Sigmoid activation function. The network’s weights are initialized using He-initialization [25].

We train the U-Net from scratch with 310 training images with a batch size of 3. Because of the limited training set size, we augment the images by horizontal flips and rotations of 90, 180, and 270 degrees, which enlarges our training set by the factor of eight. The training is terminated when the loss value of the validation set, which includes 78 images, does not decrease for 30 consecutive epochs. We use Adam optimizer with a learning rate of 0.001 to minimize the mean-squared error (MSE) loss function. The training lasted for 83 epochs and resulted in a validation MSE of 0.003 ± 0.001 . The model shows a visually consistent and accurate distance map prediction results across the validation and test data set.

In the next step, we resized the predicted distance map back to the original image size. We use bicubic interpolation to implement a smooth transformation with less distortion. We apply the different post-processing approaches, cf. Section II-C, to extract the final calving front line. The three different post-processing algorithms are parameterized as follows:

1) *Statistical Thresholding*: By setting the percentage of pixels for the threshold value for each image to 95%, most of the lower values from the distance map get removed. This results in a narrow shape mask containing our predicted calving front.

2) *Conditional Random Field*: As for the majority of the parameter values in the CRF model, we followed Chen *et al.* [13]. However, we increase the standard deviation of the Bilateral kernel to $\theta_\alpha = 512$, which overall decreases the number of artifacts and narrows the spread of the generated glacier front. We also removed the influence of the Gaussian potential, as it further reduced the width of the generated fronts and achieved the most accurate front line.

3) *Second U-Net*: The model is trained with distance maps predicted by the pixel-wise regression model with the objective

of segmenting the calving fronts. We bypass the class-imbalance problem by morphologically dilating the ground truth calving front line with a 5×5 kernel as the structuring element (SE). The same dataset split is preserved to ensure a comparable evaluation. In the optimization process, we used the Adam optimizer with the learning rate of $\text{lr} = 5e - 6$ to minimize the binary cross-entropy (BCE) loss function. We use the same U-Net architecture and initialize it analogously to the previous model. Using the same early stopping policy as before, the training took 16 epochs.

The individual approaches above show different results. In particular, the width of the predicted glacier front lines varies significantly from one approach to the other. To ensure a fair comparison, we adjusted the width of the predictions. Since both the CRF and the Second U-Net methods predict thicker glacier fronts, we reduced them for the evaluation phase. The output of the Statistical Thresholding method has a width of a single pixel (skeleton), hence we expand it accordingly. We use morphological dilation and erosion operators to adjust the width of the predicted glacier calving front lines. In the width adjustment process, we searched for the optimum structuring element (SE) size resulting in a small difference in the sum of calving front pixels for different approaches on a few test images and then applied it to the entire evaluation.

We compare our results with the state-of-the-art calving front line segmentation approach proposed by Zhang *et al.* [10], where each image is subdivided into 512×512 patches. Those are individually segmented by the U-Net. Afterwards, the output patches are combined to fit the original image size, which results in the final segmentation output. Their proposed U-Net is trained to segment the whole ice mélange and non-ice mélange regions and the calving front line is extracted via post-processing. In our application of this method, the U-Net prediction is binarized to extract the glacier and ice mélange regions. The prediction includes many artifacts. Therefore, the small holes and gaps are filled within the predicted segmentation mask using morphological closing and the remaining artifacts are removed by extracting the largest connected component (CC) and discarding the rest. The edge of this CC defines the glacier calving front line, which was automatically extracted using Canny edge detection algorithm [26]. The U-Net of Zhang *et al.* [10] is trained with the extracted patches using Adam optimizer with $\text{lr} = 1e - 5$ and the BCE loss function. Similar to our training strategy, the training was monitored by an early stopping mechanism with 30 epochs patience and converged after 103 epochs. We refer to this method as *Baseline zone*. Moreover, we also trained their U-Net architecture using only the glacier calving front line as the ground truth. We thickened the glacier calving front lines in the 512×512 ground truth image patches using a morphological dilation with a structuring element of size 5×5 . The training converged after 78 epochs. This approach is referred to as *Baseline line*.

a) *Quantitative Evaluation:* We report the dice coefficient and intersection over union (IoU) metrics. Since we try to predict a segmentation mask with a single pixel width, a small deviation in the prediction line severely affects the results leading to numerically low initial scores. We, therefore,

Score	Tolerance in meters	Zhang et al. [10]		Proposed Methods		
		Baseline zone	Baseline line	Threshold	CRF	Second U-Net
Dice	0	0.0177	0.0768	0.1176	0.1439	0.1603
	50	0.0756	0.2004	0.2656	0.3065	0.3245
	100	0.1233	0.2678	0.4043	0.4438	0.4629
	150	0.1615	0.3167	0.5233	0.5544	0.5702
	200	0.1838	0.3405	0.5908	0.6145	0.6296
	250	0.2072	0.3628	0.6529	0.6695	0.6835
IoU	0	0.0089	0.0410	0.0642	0.0795	0.0908
	50	0.0407	0.1192	0.1555	0.1826	0.1958
	100	0.0699	0.1702	0.2592	0.2891	0.3063
	150	0.0945	0.2099	0.3625	0.3893	0.4055
	200	0.1097	0.2306	0.4285	0.4500	0.4668
	250	0.1256	0.2499	0.4932	0.5096	0.5260

TABLE III: Quantitative results of the proposed methods alongside the state-of-the-art methods [10].

allow marginal deviation from the ground truth calving front line by introducing a tolerance factor. This factor defines a distance between the predicted line and the actual glacier front that will not be penalized. The tolerance is given in meters, which is translated into pixels using the individual SAR images' spatial resolution. We implement the tolerance using morphological dilation δ with a structuring element B . The structuring element's size s is determined from the tolerance value and the spatial resolution of the image. We dilate the predicted and the ground truth calving front and then calculate dice coefficient with different tolerances:

$$\text{dice}_s(y_{\text{true}}, y_{\text{pred}}) = \frac{\delta_B(y_{\text{true}}) * \delta_B(y_{\text{pred}})}{\delta_B(y_{\text{true}}) + \delta_B(y_{\text{pred}})}. \quad (5)$$

The IoU is related to the Dice coefficient by $\text{IoU} = \text{dice} / (2 - \text{dice})$ and is just given for reference.

The quantitative results can be observed in Table III. Since the manually annotated glacier calving front lines in our dataset with quality factor 1 to 4 have up to 230 meters accuracy uncertainty, we were tolerant to up to 250 meters of deviation from the ground truth line and therefore, carried out our evaluation for the wide tolerance range of 0, 50, 100, 150, 200, and 250 meters. As expected, higher tolerances consistently result in higher performance metric values. In almost all scenarios, increasing the tolerance from 0 meters to 50 meters increases the dice coefficient (and IoU) between 100% and 200%. As far as the state-of-the-art methods are concerned, training the U-Net to learn the glacier front lines directly (*Baseline line*) resulted in significantly better performance than *Baseline zone*, i.e., segmenting the ice-mélange and non-ice mélange, and extracting the boundary between them. In comparison to the state-of-the-art methods, all the proposed methods in this work outperform both *Baseline zone* and *Baseline line*. For example for the tolerance of 150 meters, the Statistical Thresholding and the Second U-Net methods achieved 0.52 and 0.57 dice coefficient while *Baseline line* obtains 0.32. Among the proposed methods, CRF and Second U-Net perform on average 7% to 11% better than the Statistical Thresholding approach. The Second U-Net shows the best quantitative results, but note that training a second network is computationally more expensive compared to the

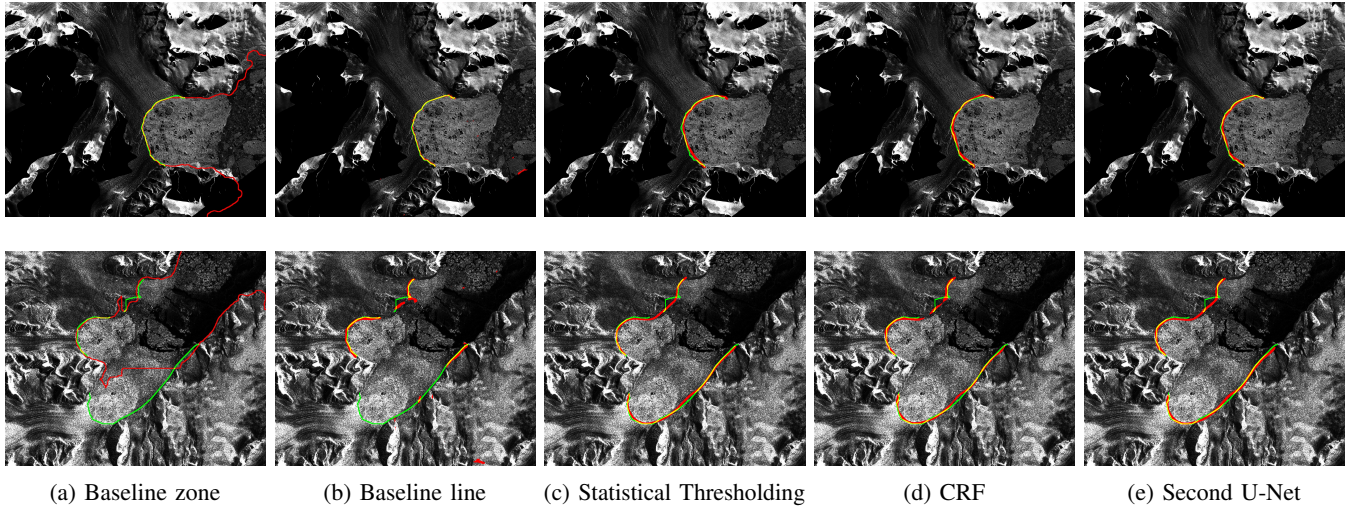


Fig. 6: Qualitative results of the different approaches for two sample glaciers. Green color represents the ground truth label, red shows the prediction, and yellow illustrates the correctly predicted pixels, i. e., the overlap between the prediction and the ground truth.

hyperparameter selection for the Statistical Thresholding and CRF approaches.

b) Qualitative Evaluation: Figure 6 depicts the automatically delineated glacier calving front positions using the proposed methods for two sample images in the test set. Each image illustrates the predicted glacier front in red, the ground truth in green, and their overlap (correct prediction) in yellow, overlaid on their corresponding SAR image. Analogous to the quantitative results, all the proposed pixel-wise regression-based models consistently predict the calving front position more accurately compared to the state-of-the-art methods. Our methods correctly predict most of the false alarms of the *Baseline zone* and *Baseline line* approaches and do not suffer from severe pollution due to outliers in the predictions. Among our proposed methods, the shape and structure of the glacier calving fronts generated by the Thresholding method are often simpler than the other two delineation approaches. The Second U-Net post-processor shows the best qualitative results since its prediction closely matches the manually annotated calving front, which is backed up consistently with our quantitative evaluation results.

Figure 7b highlights the mispredictions by the *Baseline line* method [10], which are corrected by the Second U-Net approach proposed in this work, see Fig. 7d. The state-of-the-art approach output suffers from visible artifacts, which are far off from the ground truth and do not represent the actual calving front. Further, the many green areas show the inconsistency within the prediction. Our proposed methodology using the Second U-Net tracks the ground truth consistently and avoids false alarms.

IV. CONCLUSION

This study presents a novel deep learning-based method for automatic delineation of glacier calving fronts. The main

challenge in this application is the severe class-imbalance since the region of interest contains a very small portion of the pixels in the SAR images. In this work, we proposed to first regress the distance of each pixel to the calving front line. For this task, we optimized a convolutional neural network with a U-Net architecture, specially designed for glacier front segmentation. The resulting distance map was used to localize and then generate the predicted glacier calving front line. We proposed three different approaches as a post-processing step, namely Statistical Thresholding, CRF, and Second U-Net. It has been shown that our methodology significantly outperforms the current state-of-the-art model. The Second U-Net has exhibited the best segmentation performance, which on average improves the dice coefficient of the best state-of-the-art model by about 21%. The accuracy presented by our proposed method allows glaciologists to exploit it for glaciers' change detection and automatically monitor their evolution reliably.

REFERENCES

- [1] J. J. Fürst, G. Durand, F. Gillet-Chaulet, L. Tavard, M. Rankl, M. Braun, and O. Gagliardini, "The safety band of antarctic ice shelves," *Nature Climate Change*, vol. 6, no. 5, pp. 479–482, 2016. 1
- [2] P. Friedl, T. C. Seehaus, A. Wendt, M. H. Braun, and K. Höppner, "Recent dynamic changes after the disintegration of wordie ice shelf, antarctic peninsula," *The Cryosphere*, vol. 12, no. 4, p. 1347, 2018. 1
- [3] T. A. Scambos, J. Bohlander, C. A. Shuman, and P. Skvarca, "Glacier acceleration and thinning after ice shelf collapse in the larsen b embayment, antarctica," *Geophysical Research Letters*, vol. 31, no. 18, 2004. 1, 4
- [4] P. Friedl, F. Weiser, A. Fluhrer, and M. H. Braun, "Remote sensing of glacier and ice sheet grounding lines: A review," *Earth-Science Reviews*, vol. 201, p. 102948, 2020. 1
- [5] A. A. Robel, C. Schoof, and E. Tziperman, "Persistence and variability of ice stream grounding lines on retrograde bed slopes," *The Cryosphere*, 2016. 1
- [6] C. A. Baumhoer, A. J. Dietz, S. Dech, and C. Kuenzer, "Remote sensing of antarctic glacier and ice-shelf front dynamics—a review," *Remote Sensing*, vol. 10, no. 9, p. 1445, 2018. 1

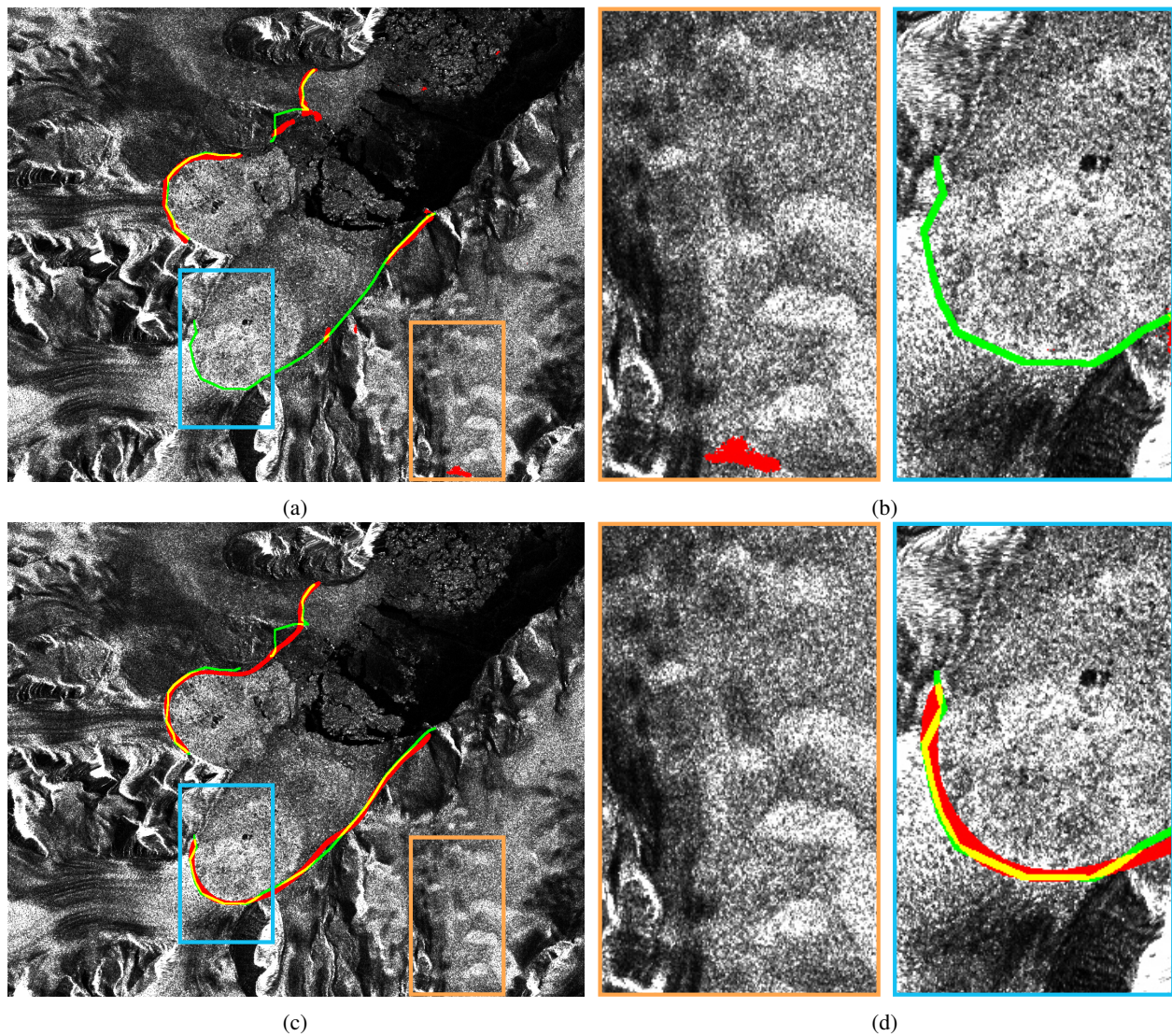


Fig. 7: Glacier calving front segmentation performance of *Baseline line* approach [10] in (a), (b) versus our proposed method using the second U-Net in (c), (d). Green color represents the ground truth label, red shows the prediction, and yellow illustrates the correctly predicted pixels, i. e., the overlap between the prediction and the ground truth.

- [7] F. Paul, N. E. Barrand, S. Baumann, E. Berthier, T. Bolch, K. Casey, H. Frey, S. Joshi, V. Konovalov, R. Le Bris, *et al.*, "On the accuracy of glacier outlines derived from remote-sensing data," *Annals of Glaciology*, vol. 54, no. 63, pp. 171–182, 2013. 1
- [8] Y. Mohajerani, M. Wood, I. Velicogna, and E. Rignot, "Detection of glacier calving margins with convolutional neural networks: A case study," *Remote Sensing*, vol. 11, no. 1, p. 74, 2019. 1
- [9] C. A. Baumhoer, A. J. Dietz, C. Kneisel, and C. Kuenzer, "Automated extraction of antarctic glacier and ice shelf fronts from sentinel-1 imagery using deep learning," *Remote Sensing*, vol. 11, no. 21, p. 2529, 2019. 1
- [10] E. Zhang, L. Liu, and L. Huang, "Automatically delineating the calving front of jakobshavn isbræ from multitemporal terrasars-x images: a deep learning approach," *The Cryosphere*, vol. 13, no. 6, pp. 1729–1741, 2019. 1, 2, 6, 7, 8
- [11] M. I. Meyer, A. Galdran, A. M. Mendonça, and A. Campilho, "A pixel-wise distance regression approach for joint retinal optical disc and fovea detection," in *International Conference on Medical Image Computing and Computer-Assisted Intervention*, pp. 39–47, Springer, 2018. 1, 2, 5
- [12] O. Ronneberger, P. Fischer, and T. Brox, "U-net: Convolutional networks for biomedical image segmentation," *CoRR*, vol. abs/1505.04597, 2015. 2
- [13] L. Chen, G. Papandreou, I. Kokkinos, K. Murphy, and A. L. Yuille, "DeepLab: Semantic image segmentation with deep convolutional nets, atrous convolution, and fully connected crfs," *CoRR*, vol. abs/1606.00915, 2016. 3, 5
- [14] P. Krähenbühl and V. Koltun, "Efficient inference in fully connected crfs with gaussian edge potentials," *CoRR*, vol. abs/1210.5644, 2012. 3
- [15] M. Oliva, F. Navarro, F. Hrbáček, A. Hernández, D. Nývlt, P. Pereira, J. Ruiz-Fernández, and R. Trigo, "Recent regional climate cooling on the antarctic peninsula and associated impacts on the cryosphere," *Science of the Total Environment*, vol. 580, pp. 210–223, 2017. 3
- [16] J. Turner, H. Lu, I. White, J. C. King, T. Phillips, J. S. Hosking, T. J. Bracegirdle, G. J. Marshall, R. Mulvaney, and P. Deb, "Absence of 21st century warming on antarctic peninsula consistent with natural variability," *Nature*, vol. 535, no. 7612, pp. 411–415, 2016. 3
- [17] A. J. Cook and D. G. Vaughan, "Overview of areal changes of the ice shelves on the antarctic peninsula over the past 50 years," *The cryosphere*, vol. 4, no. 1, pp. 77–98, 2010. 4
- [18] A. Cooper, "Historical observations of prince gustav ice shelf," *Polar Record*, vol. 33, no. 187, pp. 285–294, 1997. 4
- [19] P. Skvarca, W. Rack, H. Rott, and T. I. Y. Donángelo, "Evidence of recent climatic warming on the eastern antarctic peninsula," *Annals of Glaciology*, vol. 27, pp. 628–632, 1998. 4
- [20] H. Rott, D. Floricioiu, J. Wuite, S. Scheiblauer, T. Nagler, and M. Kern, "Mass changes of outlet glaciers along the nordensjøld coast, northern antarctic peninsula, based on tandem-x satellite measurements," *Geo-*

- physical Research Letters*, vol. 41, no. 22, pp. 8123–8129, 2014. 4
- [21] T. Seehaus, S. Marinsek, V. Helm, P. Skvarca, and M. Braun, “Changes in ice dynamics, elevation and mass discharge of dingsmoor–bombardier–edgeworth glacier system, antarctic peninsula,” *Earth and Planetary Science Letters*, vol. 427, pp. 125–135, 2015. 4
- [22] T. C. Seehaus, S. Marinsek, P. Skvarca, J. M. van Wessem, C. H. Reijmer, J. L. Seco, and M. H. Braun, “Dynamic response of sjögren inlet glaciers, antarctic peninsula, to ice shelf breakup derived from multi-mission remote sensing time series,” *Frontiers in Earth Science*, vol. 4, p. 66, 2016. 4
- [23] H. Rott, W. Abdel Jaber, J. Wuite, S. Scheiblauer, D. Floricioiu, J. M. van Wessem, T. Nagler, N. Miranda, and M. R. van den Broeke, “Changing pattern of ice flow and mass balance for glaciers discharging into the larsen a and b embayments, antarctic peninsula, 2011 to 2016,” *The Cryosphere*, vol. 12, no. 4, pp. 1273–1291, 2018. 4
- [24] A. J. Cook, T. Murray, A. Luckman, D. G. Vaughan, and N. E. Barrand, “A new 100-m digital elevation model of the antarctic peninsula derived from aster global dem: methods and accuracy assessment,” *Earth system science data*, vol. 4, no. 1, pp. 129–142, 2012. 4
- [25] K. He, X. Zhang, S. Ren, and J. Sun, “Delving deep into rectifiers: Surpassing human-level performance on imagenet classification,” in *Proceedings of the IEEE International Conference on Computer Vision (ICCV)*, December 2015. 5
- [26] J. Canny, “A Computational Approach to Edge Detection,” *IEEE Transactions on Pattern Analysis and Machine Intelligence*, vol. 8, pp. 679–698, nov 1986. 6